GEOPHYSICS, VOL. 68, NO. 4 (JULY-AUGUST 2003); P. 1241–1254, 11 FIGS., 2 TABLES.
10.1190/1.1598116

Three-dimensional imaging of multicomponent ground-penetrating radar data

J. van der Kruk*, C. P. A. Wapenaar‡, J. T. Fokkema‡, and P. M. van den Berg‡

ABSTRACT

Scalar imaging algorithms originally developed for the processing of remote sensing measurements (e.g., the synthetic-aperture radar method) or seismic reflection data (e.g., the Gazdag phase-shift method) are commonly used for the processing of ground-penetrating radar (GPR) data. Unfortunately, these algorithms do not account for the radiation characteristics of GPR source and receiver antennas or the vectorial nature of radar waves. We present a new multicomponent imaging algorithm designed specifically for vector electromagnetic-wave propagation. It accounts for all propagation effects, including the vectorial characteristics of the source and receiver antennas and the polarization of the electromagnetic wavefield. A constant-offset source-receiver antenna pair is assumed to overlie a dielectric medium. To assess the performance of the scalar and multicomponent imaging algorithms, we compute their spatial resolution function, which is defined as the image of a point scatterer at a fixed depth using a single frequency. Application of the new multicomponent imaging algorithm results in a circularly symmetric resolution function, demonstrating that the radiation characteristics of the source and receiver antennas do not influence the derived image. In contrast, the two tested scalar imaging algorithms return distinctly asymmetric resolution functions with incorrect phase characteristics, which could result in erroneous images of the subsurface when these algorithms are applied to GPR data. The multicomponent and two scalar imaging algorithms are tested on data acquired across numerous buried objects with various dielectric properties and different strike directions. Phase differences between the different images are similar to those observed in the synthetic examples. Of the tested algorithms, we conclude that the multicomponent approach produces the most reliable results.

INTRODUCTION

The shallow subsurface is of growing importance for many engineering projects, environmental issues, and archaeological investigations. As a consequence, it is often necessary to obtain images of the shallow subsurface that allow the position and character of buried objects and the composition of the host sediments or rocks to be determined. Ground-penetrating radar (GPR) is a high-resolution electromagnetic tool that has been employed successfully in numerous near-surface studies (Davis and Annan, 1989).

Because of similarities between electromagnetic and acoustic (seismic) prospecting methods, seismic imaging techniques are routinely used for the processing of GPR data (Johansson and Mast, 1994; Mast and Johansson, 1994; Grasmueck, 1996; Lehmann and Green, 1999; Binningsbø et al., 2000; Lopez-Sanchez and Fortuny-Guasch, 2000). However, there are important differences between electromagnetic and acoustic phenomena, the most significant of which is the vectorial character of electromagnetic waves compared to the scalar nature of acoustic waves. The vectorial radiation characteristics of an elementary antenna show marked angle-dependent amplitude and polarization variations (Annan et al., 1975; Engheta et al., 1982).

Recently, the radiation characteristics of elementary antennas have been taken into account during the processing of several GPR data sets. Moran et al. (2000) used a modified Kirchhoff integral by employing a half-space interfacial radiation pattern. Lehmann et al. (2000) combined coincident georadar data sets acquired with two pairs of parallel source-receiver antennas, one oriented perpendicular to the other, to obtain a "pseudoscalar" wavefield. This pseudoscalar wavefield data set was imaged using a standard 3D Kirchhoff time-migration scheme. Van Gestel and Stoffa (2000) modified a

Manuscript received by the Editor December 14, 2001; revised manuscript received November 20, 2002.
*Formerly Delft University of Technology, Centre for Technical Geoscience, Delft, The Netherlands; presently Swiss Federal Institute of Technology, Institute of Geophysics, ETH-Hoenggerberg, CH 8093 Zurich, Switzerland. E-mail: jvdkruk@aug.ig.erdw.ethz.ch.
‡Delft University of Technology, Department of Applied Earth Sciences, Mijnbouwstraat 120, 2628 RX Delft, The Netherlands. E-mail: c.p.a.wapenaar@citg.tudelft.nl; fokkema.rector@tudelft.nl.
© 2003 Society of Exploration Geophysicists. All rights reserved.

regular Kirchhoff migration algorithm by limiting the migration to those paths that fall within specified angles of orientation. All of these applications were based on scalar imaging algorithms with knowledge of the radiation characteristics of elementary GPR antennas employed heuristically to obtain improved images. Wang and Oristaglio (2000) derived a vectorial GPR imaging algorithm using the generalized Radon transform. However, they did not fully account for variations of amplitude in the forward model used in their imaging operator. Hansen and Johansen (2000) derived a vectorial inversion scheme that takes into account the planar air-soil interface. However, this scheme cannot be used for objects buried close to the interface.

A new imaging (migration) algorithm designed explicitly for electromagnetic wave phenomena is presented here. Like many imaging algorithms, it consists of two basic steps, the first of which accounts for the propagation effects of each frequency component of the electromagnetic wavefield. The so-called forward wavefield extrapolator describes the propagation of an electromagnetic wavefield from a source antenna to a receiver antenna via an arbitrary point scatterer (Figure 1). It includes the vectorial radiation characteristics of the dipole source and receiver antennas, and the polarization of the electromagnetic wavefield. The inverse wavefield extrapolator describes the reverse process (i.e., backward propagation). The second step of the imaging algorithm [the imaging principle of Claerbout (1971)] involves the summation of all backward-propagated positive and negative frequency components. It returns the final image as a pattern of physical property contrasts in the space domain.

In its present form, the new multicomponent imaging algorithm is designed to migrate wavefields scattered from objects embedded within a homogeneous half-space. Since GPR velocities are usually quite uniform over large regions, such that many investigators use a single velocity function in their processing and imaging, we suggest that computations based on arbitrary scatterers within a homogeneous half-space are reasonable first-order approximations for many GPR data sets. By properly taking into account the radiation characteristics of the antennas and the polarization of the propagating electromagnetic wavefield, markedly improved images are obtained with this algorithm.

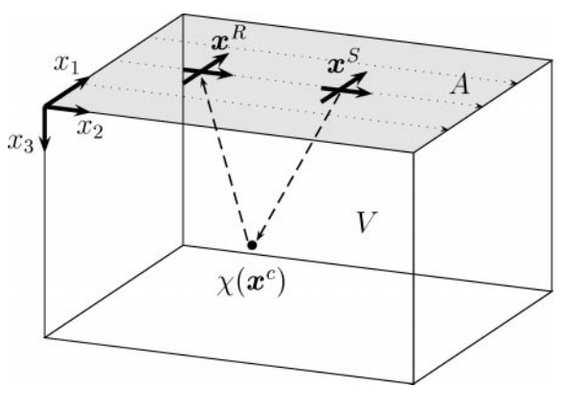

FIG. 1. Four possible source-receiver configurations on a surface A above a volume V: vector electric fields from two source antenna orientations at $\mathbf{x}^S$ can be received by two receiver antenna orientations at $\mathbf{x}^R$. Scatterer at $\mathbf{x}^c$ has physical property contrast χ.

We begin our contribution by presenting a general scattering formalism that describes the response of an arbitrary point scatterer to an incident electromagnetic wavefield. Next, we show that the scattering equation can be expressed as a convolution of the forward wavefield extrapolator with the physical property contrast between the scatterer and the host medium. After discussing multicomponent scattering in heterogeneous media and introducing multicomponent wavefield extrapolators for a homogeneous medium and a homogeneous half-space, the multicomponent inverse wavefield extrapolator is considered. At this stage, inverse wavefield extrapolators for the well-known synthetic aperture radar (SAR) and Gazdag phase-shift algorithms are also reviewed. Both of these are scalar imaging algorithms. Key aspects of the imaging principle (Claerbout, 1971) as applied to the multicomponent and scalar imaging algorithms are then examined. Finally, the performances of the imaging algorithms are tested in two ways. One test involves comparing the respective spatial resolution functions, which are defined as the images of a point scatterer in a homogeneous medium (or a homogeneous half-space) using a single frequency component. For the second test, complete three-dimensional (3D) images are computed from a complex experimental field data set.

Several critical properties of the multicomponent and the two scalar imaging algorithms are best demonstrated for the ideal case of a point scatterer located within a homogeneous medium. To maintain the flow of the paper, derivations of key equations for this simple case have been relegated to Appendices. Analytic solutions for the forward wavefield extrapolator in a homogeneous medium and a homogeneous half-space are described in Appendix A. We demonstrate in Appendix B that inverse wavefield extrapolators derived for individual components of the forward wavefield extrapolator in a homogeneous medium have unbounded amplitudes. Similar conclusions can also be drawn for the equivalent half-space problem. Finally, analytic representations for the spatial resolution functions of the tested imaging algorithms are derived in Appendix C. Although the homogeneous full-space model is not physically plausible, it allows us to demonstrate in a straightforward manner the limitations and potential of the multicomponent and two scalar imaging algorithms.

SCATTERING FORMALISM FOR AN ARBITRARY HETEROGENEOUS MEDIUM

We begin by assuming that we can deploy our source and receiver antennas in two different orientations, thus providing the possibility of four source-receiver configurations (Figure 1). The linearized expression for the scattering formalism based on the Born approximation is given by

$$\hat{E}^s_\alpha(\mathbf{x}^R, \mathbf{x}^S, \omega) = \int_{V(\mathbf{x}^c)} \hat{G}_{\alpha\ell}(\mathbf{x}^R|\mathbf{x}^c, \omega)\chi(\mathbf{x}^c) \times \hat{G}_{\ell\beta}(\mathbf{x}^c|\mathbf{x}^S, \omega)\hat{J}_\beta(\mathbf{x}^S, \omega)\,\mathrm{d}V, \quad (1)$$

where $\omega = 2\pi f$, $\hat{}$ indicates the space-frequency domain, $V(\mathbf{x}^c)$ is the scattering volume, $\mathbf{x} = (x_1, x_2, x_3)$ with x_3 increasing downwards, and Einstein's summation convention applies to repeated subscripts; Latin subscripts can take values $\{1, 2, 3\}$, whereas Greek subscripts can take values $\{1, 2\}$. The Green's function $\hat{G}_{\ell\beta}(\mathbf{x}^c|\mathbf{x}^S, \omega)$ describes the propagation of the vectorial electric field emitted by a point source $\hat{J}_\beta$ (electric

current density) at position $\mathbf{x}^S$ to a scatterer with physical property contrast χ at position $\mathbf{x}^c$ (Figure 1). This scatterer can be considered as a secondary source, such that the propagation from $\mathbf{x}^c$ towards the receiver at $\mathbf{x}^R$ is described by $\hat{G}_{\alpha\ell}(\mathbf{x}^R|\mathbf{x}^c, \omega)$. Both Green's functions include the vectorial radiation characteristics of the dipole antennas. The contrast χ is defined as $\chi = \hat{\eta}^s - \hat{\eta}$, where $\hat{\eta}^s$ and $\hat{\eta}$ describe the physical properties of the scatterer and background, respectively. The quantity $\hat{\eta}$ is defined as $\hat{\eta} = \sigma + j\omega\varepsilon$, where j is $\sqrt{-1}$, σ is the conductivity, and ε is the permittivity. It is convenient to regard the contrast χ as a complex conductivity contrast, where the imaginary part of the complex conductivity indicates a permittivity contrast. The point source can be described by

$$\hat{J}_\beta = \hat{S}(\omega) b_\beta, \tag{2}$$

where $\hat{S}(\omega)$ is the source wavelet, and b_1 and b_2 identify two source antenna orientations, one along the x_1-direction and one along the x_2-direction (Figure 1). We assume that the source and receiver are present on the same horizontal plane, $x_3^S = x_3^R = 0$.

FORWARD WAVEFIELD EXTRAPOLATOR

Heterogeneous medium

To simplify the inverse formulation discussed later in the text, we introduce a translated coordinate system defined by the midpoints $\mathbf{x}^M = (\mathbf{x}^S + \mathbf{x}^R)/2$ and the half-offsets $\mathbf{x}^H = (\mathbf{x}^R - \mathbf{x}^S)/2$. Because four different source-receiver combinations are possible, we introduce $\hat{E}_{\alpha\beta}(\mathbf{x}^M, \mathbf{x}^H, \omega)$:

$$\hat{E}^s_\alpha(\mathbf{x}^R, \mathbf{x}^S, \omega) = \hat{E}_{\alpha\beta}(\mathbf{x}^M, \mathbf{x}^H, \omega) b_\beta, \tag{3}$$

where $\hat{E}_{\alpha\beta}$ is given by

$$\hat{E}_{\alpha\beta}(\mathbf{x}^M, \mathbf{x}^H, \omega) = \hat{S}(\omega) \int_{V(\mathbf{x}^c)} \hat{D}_{\alpha\beta}(\mathbf{x}^M, \mathbf{x}^H|\mathbf{x}^c, \omega) \chi(\mathbf{x}^c)\, \mathrm{d}V, \tag{4}$$

and the forward wavefield extrapolator $\hat{D}_{\alpha\beta}$ is defined as the inner product of the Green's function describing downward propagation from the source towards the scatterer and the Green's function describing upward propagation from the scatterer towards the receiver:

$$\begin{aligned}\hat{D}_{\alpha\beta}&(\mathbf{x}^M, \mathbf{x}^H|\mathbf{x}^c, \omega)\\ &= \hat{G}_{\alpha\ell}(\mathbf{x}^M + \mathbf{x}^H|\mathbf{x}^c, \omega)\hat{G}_{\ell\beta}(\mathbf{x}^c|\mathbf{x}^M - \mathbf{x}^H, \omega),\\ &= \hat{G}_{\alpha\ell}(\mathbf{x}^M + \mathbf{x}^H|\mathbf{x}^c, \omega)\hat{G}_{\beta\ell}(\mathbf{x}^M - \mathbf{x}^H|\mathbf{x}^c, \omega).\end{aligned} \tag{5}$$

Note that equations (4) and (5) are valid for arbitrary media.

In equation (4), the measured electric field is a spatial convolution of the forward wavefield extrapolator with the physical contrast properties. We aim to find an inverse wavefield extrapolator that compensates for the propagation effects described by the forward wavefield extrapolator. Consequently, it is convenient to perform a horizontal spatial Fourier transformation, so that convolutions in the space-frequency ($\mathbf{x}$-ω) domain become multiplications in the wavenumber-frequency ($\mathbf{k}$-ω) domain (actually the k_1k_2-x_3-ω domain). Later, the forward wavefield extrapolators in a homogeneous medium and a homogeneous half-space will be analyzed in both the $\mathbf{x}$-ω and $\mathbf{k}$-ω domains.

A multicomponent scattering formalism is achieved by converting equation (4), which describes the components $\hat{E}_{\alpha\beta}$ individually, into a matrix:

$$\hat{\mathbf{E}}(\mathbf{x}^M, \mathbf{x}^H, \omega) = \hat{S}(\omega) \int_{V(\mathbf{x}^c)} \hat{\mathbf{D}}(\mathbf{x}^M, \mathbf{x}^H|\mathbf{x}^c, \omega) \chi(\mathbf{x}^c)\, \mathrm{d}V, \tag{6}$$

where the matrix $\hat{\mathbf{E}}(\mathbf{x}^M, \mathbf{x}^H, \omega)$ contains the four scattered electric field values that are generated and measured by the four possible source-receiver combinations (Figure 1). It is given by

$$\hat{\mathbf{E}}(\mathbf{x}^M, \mathbf{x}^H, \omega) = \begin{bmatrix} \hat{E}_{11}(\mathbf{x}^M, \mathbf{x}^H, \omega) & \hat{E}_{12}(\mathbf{x}^M, \mathbf{x}^H, \omega) \\ \hat{E}_{21}(\mathbf{x}^M, \mathbf{x}^H, \omega) & \hat{E}_{22}(\mathbf{x}^M, \mathbf{x}^H, \omega) \end{bmatrix}, \tag{7}$$

and the corresponding forward wavefield extrapolator is given by

$$\begin{aligned}&\hat{\mathbf{D}}(\mathbf{x}^M, \mathbf{x}^H|\mathbf{x}^c, \omega)\\ &\quad= \begin{bmatrix} \hat{D}_{11}(\mathbf{x}^M, \mathbf{x}^H|\mathbf{x}^c, \omega) & \hat{D}_{12}(\mathbf{x}^M, \mathbf{x}^H|\mathbf{x}^c, \omega) \\ \hat{D}_{21}(\mathbf{x}^M, \mathbf{x}^H|\mathbf{x}^c, \omega) & \hat{D}_{22}(\mathbf{x}^M, \mathbf{x}^H|\mathbf{x}^c, \omega) \end{bmatrix}.\end{aligned} \tag{8}$$

Homogeneous medium and homogeneous half-space

The forward wavefield extrapolators in a homogeneous medium and a homogeneous half-space for the four zero-offset source-receiver antenna configurations ($\mathbf{x}^S = \mathbf{x}^R = \mathbf{x}^M$, $\mathbf{x}^H = 0$) are given in Appendix A. Following from equations (6)–(8), the wavefield extrapolators for the four source-receiver configurations may be combined, such that the multicomponent forward wavefield extrapolator may be written in matrix form as follows:

$$\hat{\mathbf{D}}(\mathbf{x}, \omega) = \hat{\mathbf{A}}(\mathbf{x}, \omega) \exp(-2jkR), \tag{9}$$

where

$$\hat{\mathbf{A}}(\mathbf{x}, \omega) = \begin{bmatrix} \hat{A}_{11}(\mathbf{x}, \omega) & \hat{A}_{12}(\mathbf{x}, \omega) \\ \hat{A}_{21}(\mathbf{x}, \omega) & \hat{A}_{22}(\mathbf{x}, \omega) \end{bmatrix}. \tag{10}$$

For a homogeneous medium, $\hat{A}_{\alpha\beta}$ is given by equation (A-3).

Following the derivation of equation (A-7) in Appendix A, equation (9) in the wavenumber-frequency domain is obtained by carrying out a horizontal spatial Fourier transformation that results in

$$\tilde{\mathbf{D}}(k_1, k_2, x_3, \omega) = \tilde{\mathbf{d}}(k_1, k_2, x_3, \omega) \exp(-jk_3|x_3|), \tag{11}$$

where for a homogeneous medium

$$\tilde{\mathbf{d}}(k_1, k_2, x_3, \omega) = \frac{-2\pi jC(\omega)}{(2k)^3|x_3|} \begin{bmatrix} (2k)^2 - k_1^2 & -k_1k_2 \\ -k_1k_2 & (2k)^2 - k_2^2 \end{bmatrix}. \tag{12}$$

For a homogeneous half-space, expressions for $\tilde{\mathbf{d}}$ are more complicated.

INVERSE WAVEFIELD EXTRAPOLATORS

The ideal inverse wavefield extrapolator should compensate for the effects of the forward wavefield extrapolator. The symbol $\hat{H}$ will be used to describe the different inverse wavefield extrapolators. We begin with the simplest situation, that of zero-offset source and receiver antennas within a homogeneous medium.

Multicomponent inverse wavefield extrapolator for a zero-offset source-receiver antennas within a homogeneous medium

The multicomponent inverse wavefield extrapolator is obtained by inverting the expression for the multicomponent forward wavefield extrapolator in the $\mathbf{k}$-ω domain (equation (11). The inverse wavefield extrapolator is only determined in the propagating wave region; evanescent waves are ignored. This is achieved by taking the complex conjugate of the exponent in equation (11) and the inverse of the matrix in equation (12):

$$\tilde{\mathbf{H}}^{mc}(k_1, k_2, x_3, \omega) = \tilde{\mathbf{h}}^{mc}(k_1, k_2, x_3, \omega)\exp\left(jk_3^*|x_3|\right), \tag{13}$$

where * denotes complex conjugate and

$$\tilde{\mathbf{h}}^{mc}(k_1, k_2, x_3, \omega) = \frac{jk|x_3|}{\pi C(\omega)k_3^2}\begin{bmatrix}(2k)^2 - k_2^2 & k_1k_2 \\ k_1k_2 & (2k)^2 - k_1^2\end{bmatrix}. \tag{14}$$

Using the stationary phase approximation, the spatial equivalent of equations (13) and (14) is obtained as

$$\hat{\mathbf{H}}^{mc}(\mathbf{x}, \omega) = \frac{4k^2}{4\pi^2 C(\omega)} \times \begin{bmatrix}\left(R^2 - x_2^2\right)/R^2 & x_1x_2/R^2 \\ x_1x_2/R^2 & \left(R^2 - x_1^2\right)/R^2\end{bmatrix}\exp(2jkR). \tag{15}$$

A simple relation between $\hat{\mathbf{D}}$ and $\hat{\mathbf{H}}^{mc}$ is given by

$$\hat{\mathbf{H}}^{mc}(\mathbf{x}, \omega) = -\frac{R^2k^2}{\pi^2C^2}\begin{bmatrix}0 & 1 \\ -1 & 0\end{bmatrix}\hat{\mathbf{D}}^H(\mathbf{x}, \omega)\begin{bmatrix}0 & 1 \\ -1 & 0\end{bmatrix}, \tag{16}$$

where ^{H} denotes the Hermitian (conjugate transpose) operator.

By treating the problem in this manner, single elements of the multicomponent inverse wavefield extrapolator are bounded [see equation (15)], which contrasts markedly with the unbounded wavefield extrapolators derived in Appendix B. We see now that the conversion of the individual-component representation of equation (4) to the explicitly combined matrix representation of equation (6) is a critical step. Our multicomponent inverse wavefield extrapolator [equations (13)–(15)] is a suitable approximate inverse of the forward wavefield extrapolator that takes into account the vectorial radiation characteristics of the dipole antennas and the propagating wavefield.

Multicomponent inverse wavefield extrapolator for common-offset source-receiver antennas on the surface of a homogeneous half-space

For a homogeneous half-space, an inverse wavefield extrapolator cannot be analytically derived. This is due to the complicated nature of the amplitudes of the forward wavefield extrapolator (see discussion in Appendix A). Nevertheless, an inverse wavefield extrapolator can be determined using numerical methods. An important secondary benefit of numerical methods is that offsets between the source and receiver antennas can be taken into account.

For this case, the Green's functions in equation (5) that contribute to the forward wavefield extrapolator of equation (8) describe the propagation of an electric field in a homogeneous half-space (Engheta et al., 1982). To obtain the inverse wavefield extrapolator, the inner product of the two Green's functions is determined for each midpoint position $\mathbf{x}^M$. Subsequently, a two-dimensional spatial Fourier transformation is carried out. An inverse matrix is then numerically estimated for each k_1-k_2 combination, resulting in a representation of the inverse extrapolator in the $\mathbf{k}$-ω domain. As for the homogeneous case, the inverse wavefield extrapolator is only determined in the propagating wave region; the evanescent wave region is ignored.

SAR and Gazdag scalar inverse wavefield extrapolators

Unlike the individual inverse wavefield extrapolators discussed in Appendix B (which have unbounded amplitudes), the conventional SAR and Gazdag scalar inverse wavefield extrapolators do not consider the vector characteristics of GPR propagation and do not include amplitude information in the domains in which they are defined. SAR imaging was originally developed for remote sensing (Curlander and McDonough, 1991). The SAR inverse wavefield extrapolator is defined in the $\mathbf{x}$-ω domain by the complex conjugate of the phase shift in equation (9). Its equivalent in the $\mathbf{k}$-ω domain is conveniently determined using the method of stationary phase. The SAR inverse extrapolators in the $\mathbf{x}$-ω and $\mathbf{k}$-ω domains are

$$\hat{H}^{sar} = \exp(j2kR), \tag{17}$$

$$\tilde{H}^{sar} = \frac{4\pi jk|x_3|}{\left(k_3^*\right)^2}\exp\left(jk_3^*|x_3|\right). \tag{18}$$

With k_3 defined by equation (A-8), $\exp(jk_3^*|x_3|)$ is bounded for all k_1 and k_2. In the seismic literature, imaging based on this extrapolator is known as diffraction-summation migration.

The inverse wavefield extrapolator that forms the basis for Gazdag phase-shift migration [see equation (45) of Gazdag (1978)] is defined in the $\mathbf{k}$-ω domain by the complex conjugate of the phase term in equation (11). Its equivalent in the $\mathbf{x}$-ω is determined by the method of stationary phase. The Gazdag inverse extrapolators in the $\mathbf{x}$-ω and $\mathbf{k}$-ω domain are

$$\hat{H}^{gd} = \frac{-jk|x_3|}{\pi R^2}\exp(2jkR), \tag{19}$$

$$\tilde{H}^{gd} = \exp\left(jk_3^*|x_3|\right). \tag{20}$$

The SAR and Gazdag extrapolators represent simple phase shifts in the $\mathbf{x}$-ω and $\mathbf{k}$-ω domains, respectively.

IMAGING PRINCIPLE

The imaging principle of Claerbout (1971) involves determining a time zero for each position via a summation of all positive and negative frequency components. This allows us to write for the imaged contrast at a specific depth:

$$\langle\chi(\mathbf{x})\mathbf{I}\rangle^{mc} = \frac{1}{2\pi}\int\frac{\mathrm{d}\omega}{\hat{S}(\omega)} \times \int_{A\left(x_1^M, x_2^M\right)}\hat{\mathbf{H}}^{mc}(\mathbf{x} - \mathbf{x}^M, \omega)\hat{\mathbf{E}}(\mathbf{x}^M, \omega)\,\mathrm{d}A, \tag{21}$$

where $\mathbf{I}$ is the unity matrix and ^{mc} refers to the multicomponent inverse wavefield extrapolator. The approximate inverse

of the multicomponent forward wavefield extrapolator $\hat{\mathbf{D}}$ (see equation (6)], which is given by $\hat{\mathbf{H}}^{mc}$, accounts for all traveltimes and amplitudes associated with a wave traveling through a homogeneous medium or homogeneous half-space, including the vectorial radiation characteristics of the (point) source and (point) receiver. The diagonal components $\langle\chi(\mathbf{x})\mathbf{I}\rangle_{11}^{mc}$ and $\langle\chi(\mathbf{x})\mathbf{I}\rangle_{22}^{mc}$ both return estimated values of the imaged contrast (see also Appendix C). According to equation (21), each diagonal component consists of a summation of two different measurements ($\hat{E}_{11}$ and $\hat{E}_{21}$ or $\hat{E}_{12}$ and $\hat{E}_{22}$), which are imaged separately by using appropriate inverse wavefield extrapolators ($\hat{H}_{11}^{mc}$ and $\hat{H}_{12}^{mc}$ or $\hat{H}_{21}^{mc}$ and $\hat{H}_{22}^{mc}$). It is interesting to note that the multicomponent formulation required consideration of four components, whereas for an omnidirectional scatterer only two measurements are required, because the two diagonal components of $\langle\chi(\mathbf{x})\mathbf{I}\rangle$ return identical results when the reflection coefficients are equal. This may not always be the case. By analyzing the diagonal results separately, additional information about the reflectivity of the scatterer may be obtained.

By replacing the inverse multicomponent wavefield extrapolator in equation (21) with the respective scalar inverse wavefield extrapolators [equations (17) and (19)], the SAR and Gazdag image contrasts are obtained.

SPATIAL RESOLUTION FUNCTIONS

Spatial resolution functions in a homogeneous medium

The performances of the 3D multicomponent and conventional scalar inverse wavefield extrapolators are investigated by analyzing images of a point scatterer using a single frequency component. These images are a form of spatial resolution function. The spatial resolution functions are examined for a point scatterer with a real-valued (conductivity) contrast with unit amplitude. We first assume that a zero-offset source-receiver configuration measures on a plane within a homogeneous medium. Closed-form expressions for the forward and inverse wavefield extrapolators in the $\mathbf{x}$-ω and $\mathbf{k}$-ω domains enable the derivation of closed-form expressions for the spatial resolution functions of the multicomponent and Gazdag imaging algorithms (Appendix C). In this way, analytical checks of the inverse wavefield extrapolators' performances can be made. A summary of the results for the different inverse wavefield extrapolators derived in Appendix C is given in Table 1. Since a closed-form expression for the SAR inverse wavefield extrapolator cannot be derived, the widths of its main lobes cannot be analytically determined.

The multicomponent extrapolator returns a real-valued circularly symmetric resolution function with a positive peak [equation (C-6)]. It correctly represents the properties of the point scatterer. Equal spatial resolutions for the x_1- and x_2-axes are obtained, whereas for the Gazdag inverse extrapolator better resolution is obtained along the x_2-axis than along the x_1-axis. The SAR extrapolator produces a negative real value, and the Gazdag extrapolator produces a positive imaginary value. The negative/imaginary values of the amplitude peaks obtained using the two scalar inverse extrapolators do not represent the properties of the point scatterer, which has a positive real-valued contrast [note, that C in equation (A-4) has a negative value]. In addition, both the SAR and the Gazdag extrapolators return a noncircularly symmetric resolution function, and the amplitude of the spatial resolution function obtained using the Gazdag extrapolator depends on the depth of the diffractor. This demonstrates that, in contrast to the images obtained with the multicomponent imaging algorithm, those obtained with the scalar extrapolators are influenced by the radiation characteristics of the source and receiver antennas and thus do not represent accurately the nature of the physical property contrast.

Table 1. Width of the main lobe (measured at the first zero) for the spatial resolution functions at the depth level of the diffractor using the closed-form expressions (where available).

Inverse extrapolator	Width of the main lobe		Amplitude proportional to
	x_1-axis	x_2-axis	
Multicomponent	0.64λ	0.64λ	$k/2\pi$
SAR			$C/2k$
Gazdag	0.84λ	0.60λ	$-jC/\lvert x_3^d\rvert$

Spatial resolution function in a homogeneous half-space

It is not feasible to derive closed-form expressions for the spatial resolution functions when a point scatterer is present within a homogeneous half-space. This is due to the complicated radiation characteristics of a horizontal dipole present on a dielectric half-space. Consequently, numerical methods using far-field expressions for these radiation patterns are employed (Engheta et al., 1982). We compute the scattered electric field by using the far-field expressions for a 1-m-deep buried point scatterer with a real-valued contrast of unit amplitude. The inverse wavefield extrapolator is derived numerically using the same far-field expressions.

Figure 2 shows the normalized (absolute maximum value is set to 1) real and imaginary parts of the spatial resolution functions that were obtained by using the multicomponent, SAR, and Gazdag inverse wavefield extrapolators, respectively. The normalized real and imaginary parts of the spatial resolution function obtained by using the multicomponent inverse wavefield extrapolator show a realistic positive real-valued image of the point scatterer. Both scalar imaging algorithms produce noncircularly symmetric resolution functions with nonzero imaginary contrasts. The SAR extrapolator produces dominantly negative real and relatively weak imaginary values. By comparison, the Gazdag extrapolator produces strong positive imaginary values and relatively weak real values. The negative and imaginary values shown in the center and right diagrams of Figure 2 do not represent the properties of the point scatterer, which has a positive real-valued contrast. These results are similar to those obtained from the analysis for the homogeneous medium (see Table 1). Note that there are markedly larger oscillations in the tails of the scalar spatial resolution functions than in the tails of the multicomponent spatial resolution function. From these synthetic results, we conclude that only the multicomponent imaging algorithm is capable of producing images that allow the magnitudes and types of low physical contrasts to be distinguished.

EXPERIMENTAL RESULTS

Description of the measurements

For the controlled experiments, a testing site was constructed at Scheveningen near The Netherlands coast. Several steel

pipes with various orientations with respect to the survey lines and one plastic and several metallic spheres were buried in a large sandbox. The positions of the objects are shown schematically in Figure 3 and the properties are given in Table 2. Measurements were made across a 3 × 4 m area using a pulse EKKO 1000 system with 900-MHz antennas (Figure 4).

To ensure that the antenna offsets and alignments remained fixed, a rigid frame was constructed. This frame enabled data to be recorded with four source-receiver orientations (Figure 5). Offsets between the source and the receiver were always parallel to the survey line. Commonly used terms for describing the various source-receiver antenna configurations (perpendicular broadside, perpendicular-parallel inline, parallel-perpendicular in-line, and parallel endfire) are explained in Figure 5.

Table 2. Overview of the properties of the buried objects.

Object	Material	Length (cm)	Diameter (cm)	Position (top) x_1, x_2, x_3 (cm)
A	Metal pipe	100.0	15.9	(140, 95, 40) (240, 95, 43)
B	Metal pipe	100.0	22.3	(140, 55, 42) (240, 55, 40)
C	Metal pipe	99.5	6.2	(−35, 75, 15) (55, 75, 53)
D	Metal sphere		19.1	(35, 250, 53)
E	Metal sphere		19.1	(35, 290, 55)
F	Plastic sphere		21.0	(145, 273, 45)
G	Metal pipe	185.0	9.0	(235, 325, 50) (372, 449, 50)

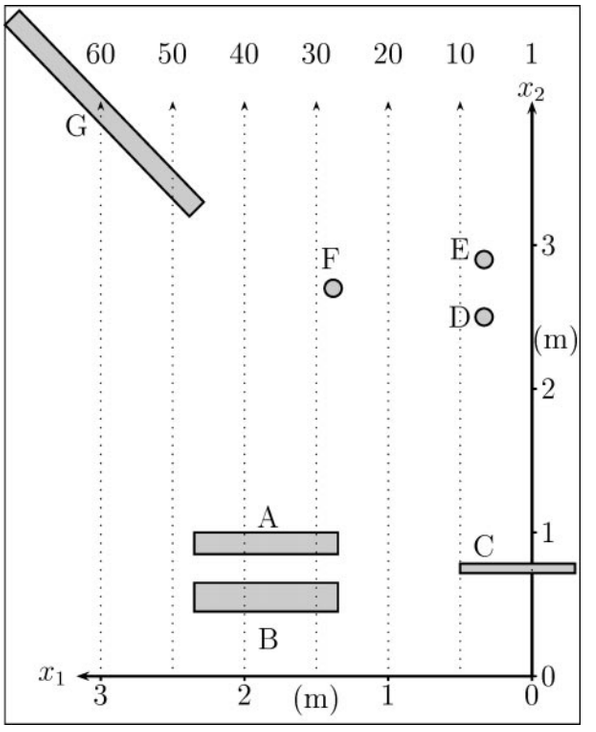

FIG. 3. Plan view of buried objects at the testing site (coordinates of objects are given in Table 2). Numbers refer to lines along which GPR data were acquired.

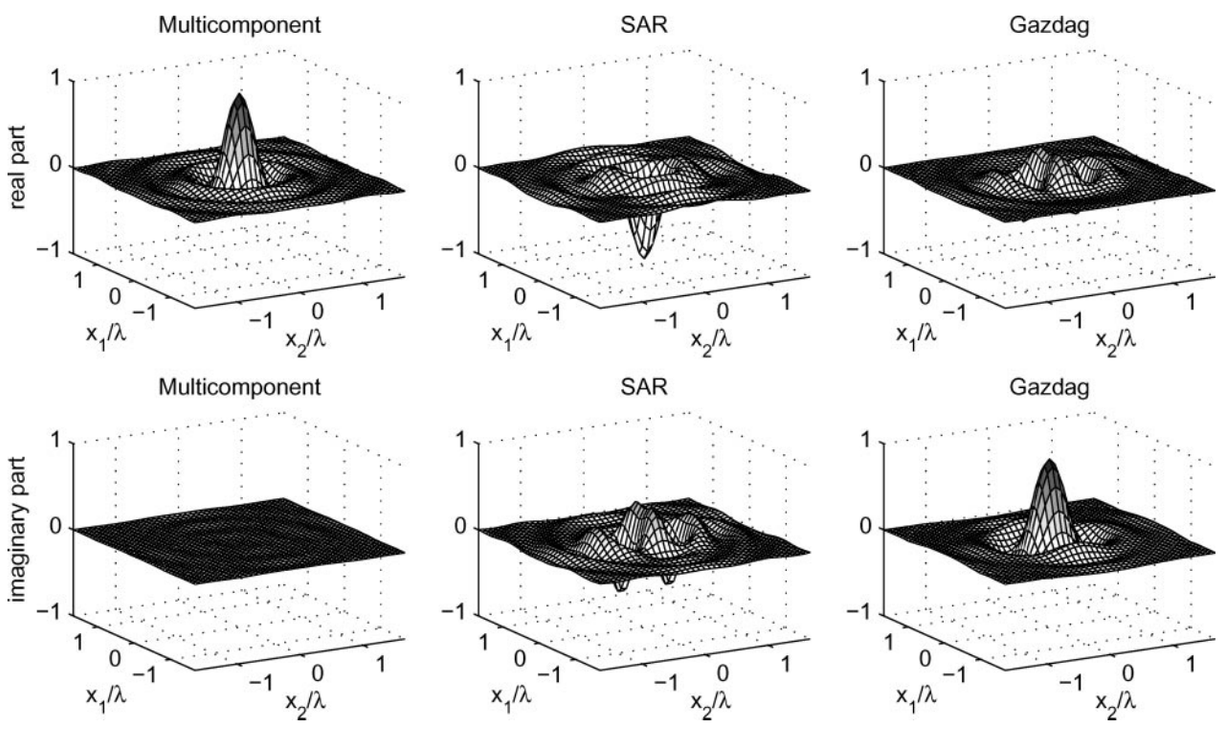

FIG. 2. Normalized real and imaginary parts of spatial resolution functions computed for the multicomponent, SAR, and Gazdag inverse extrapolators. See text for definition of spatial resolution functions.

The multicomponent measurements were carried out on a survey grid consisting of 60 lines oriented in the x_2-direction. Inline and crossline spatial sampling was set to $\Delta x_1^M = \Delta x_2^M = 5$ cm. The offset between the source and receiver antennas was maintained at $2\Delta x_2^H = 35$ cm, a separation that ensured no clipping of the measured electric field. A vertical stacking of 16 was used. Temporal sampling was 50 ps, and the total recording time was 50 ns.

FIG. 4. The 3×4 m test area within which the multicomponent measurements were made.

3D imaging results

Initially, static corrections that involve aligning the maximum and minimum values of the direct air wave are applied. Our imaging algorithm assumes that only scattered signals are recorded. In reality, direct air and ground waves are also recorded. To remove these direct waves, which have a constant waveform in the case of a homogeneous top layer, simple subtraction of an average trace is carried out.

The data are imaged using an effective relative permittivity for the lower homogeneous half-space of $\varepsilon_r = 3.1$. The radiation patterns in a homogeneous half-space and the offset between the source and receiver antennas are taken into account. Examining separately the real and imaginary parts of the spatial resolution functions is an effective way to analyze the characteristics of the diffferent imaging algorithms. When the imaging is carried out by summing all positive and negative frequency components [e.g. equation (21)], the information present in the imaginary part will not be available. This is caused by the fact

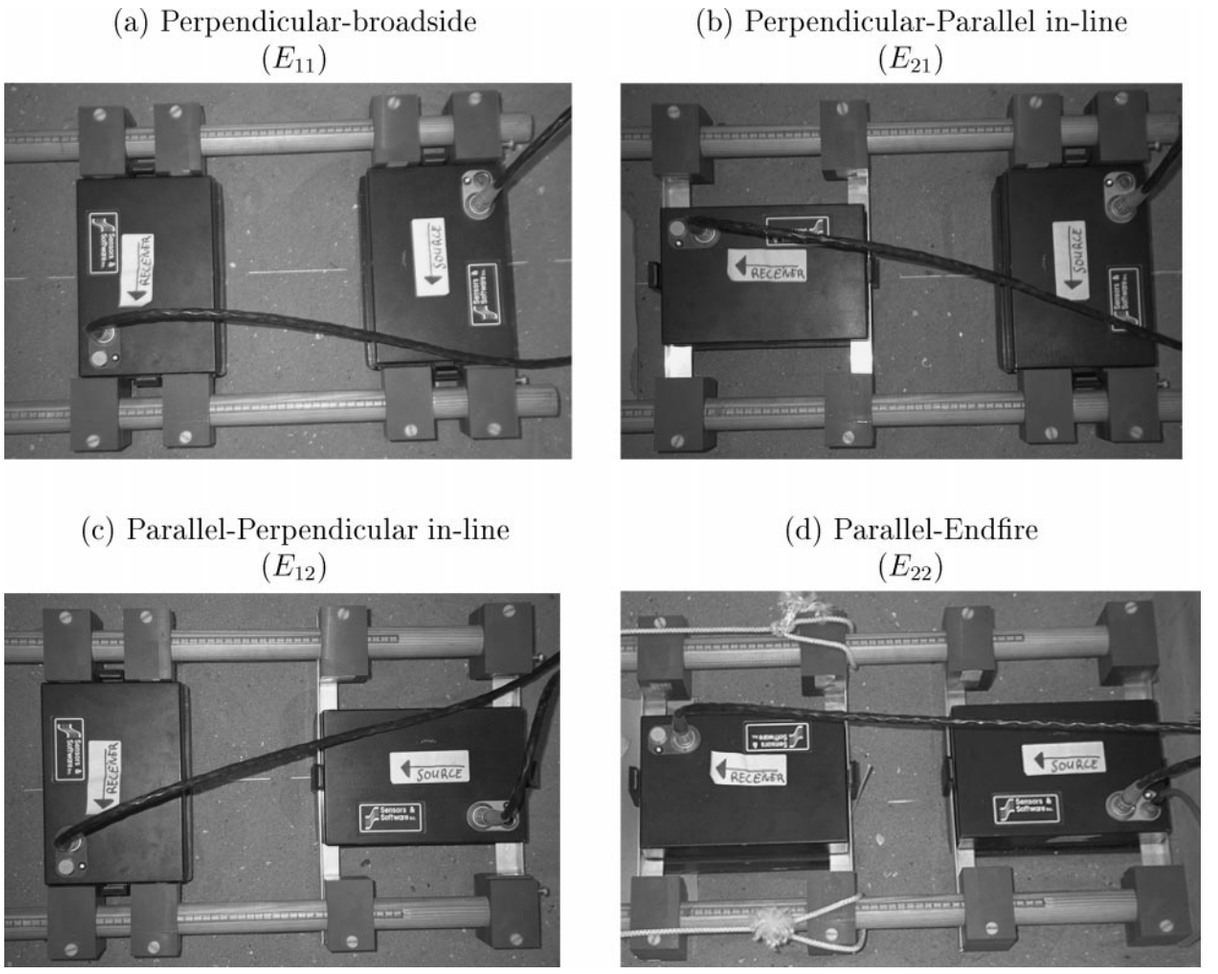

FIG. 5. Four in-line configurations attached to a rigid frame used for the multicomponent experiments with a source-receiver offset of 35 cm.

that the positive frequency components are the conjugates of the negative ones. Therefore, the experimental imaging results will be analyzed using only the positive frequencies.

The imaging described by equation (21) was performed by summing 45 positive frequency components over the range 100–960 MHz. In our analysis, the source wavelet was not taken into account. As a consequence, the properties of the scattered objects could not be extracted. Nevertheless, separate analyses of the real and imaginary parts of the images allowed the performances of the different imaging algorithms to be assessed.

Multicomponent measurements were carried out using the four inline source-receiver combinations displayed in Figure 5. Using the multicomponent imaging algorithm, the perpendicular-broadside configuration (E_{11}) and the perpendicular-parallel in-line configuration (E_{21}) measurements were combined to yield the contrast $\langle\chi(\mathbf{x})\mathbf{I}\rangle_{11}^{mc}$ in equation (21). Similarly, the scattered electric field measured in the parallel-perpendicular in-line (E_{12}) and the parallel-endfire (E_{22}) configurations were combined to give the contrast $\langle\chi(\mathbf{x})\mathbf{I}\rangle_{22}^{mc}$. The imaging results $\langle\chi(\mathbf{x})\mathbf{I}\rangle_{22}^{mc}$ were of noticeably lower quality than those of $\langle\chi(\mathbf{x})\mathbf{I}\rangle_{11}^{mc}$. Markedly different degrees of overlap between the source antenna footprint and receiver antenna footprint provides a possible explanation for this observation. The overlap of source and receiver footprints for the perpendicular-broadside configuration (E_{11}) is larger than the overlap for the parallel-endfire configuration (E_{22}), resulting in higher amplitudes of the former configuration than for the latter. Because of the relatively low quality of the $\langle\chi(\mathbf{x})\mathbf{I}\rangle_{22}^{mc}$ results, we only show the $\langle\chi(\mathbf{x})\mathbf{I}\rangle_{11}^{mc}$ results, which consist of a real and an imaginary part at each position in the image domain.

Equiamplitude surfaces for the multicomponent imaging results in a 3D volume

To obtain an overall picture of the results, surfaces of constant absolute value in the image domain were used to depict the different objects. The thresholds for these surfaces of constant amplitude were chosen according to the maximum amplitudes of the objects. Because the different objects produced different maximum amplitudes, different thresholds were used. These are indicated in Figure 6a for the multicomponent imaging results $\langle\chi(\mathbf{x})\mathbf{I}\rangle_{11}^{mc}$. In Figures 6b and 6c, the results are depicted for other observation angles. The metal pipes A and B have the largest amplitudes and the plastic sphere F has the smallest. Some unexplained anomalies that have amplitudes comparable to that of the plastic sphere F are also present. Because all information is contained in these pictures, they represent well the structural characteristics of the imaged objects. However, since the source wavelet characteristics have not been determined, this analysis provides little useful information on their physical properties.

Comparison between the imaging algorithms in different planes

For the homogeneous medium and half-space, we have shown that the SAR and Gazdag algorithms return images

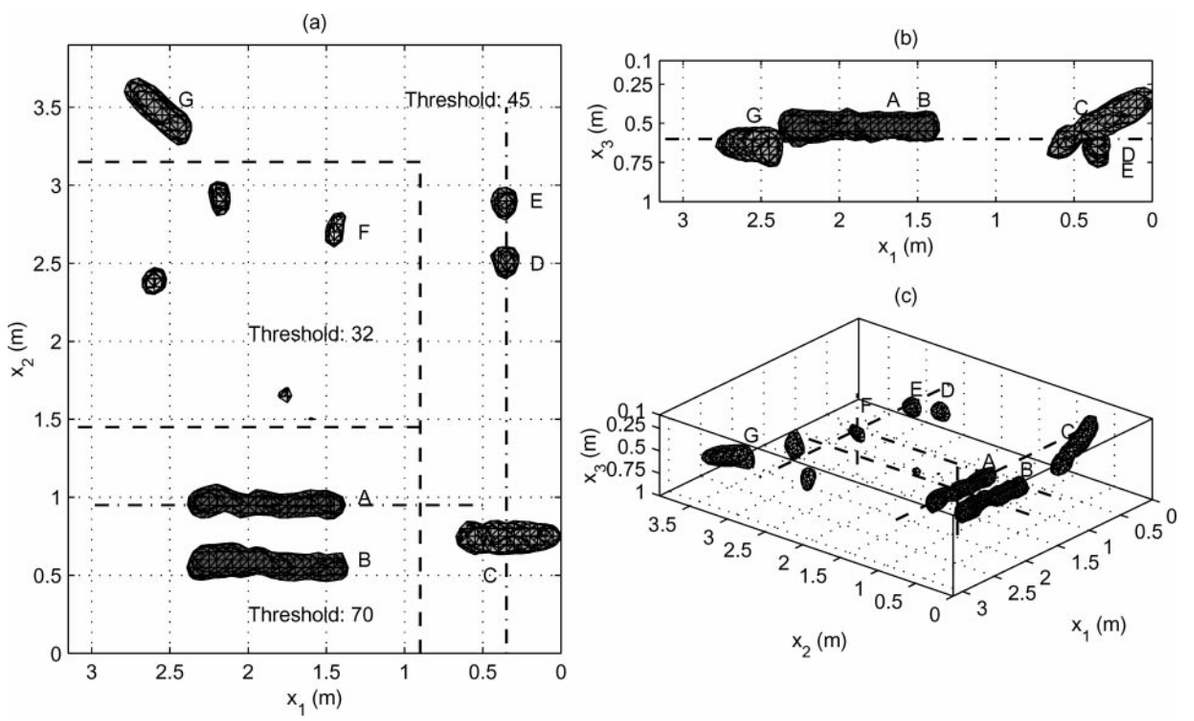

FIG. 6. Three different views of multicomponent images determined from data recorded using pulseEKKO 1000 900-MHz antennas in the perpendicular-broadside and perpendicular-parallel inline configurations (Figure 5). The dashed lines in (a) delineate the three threshold regions. The dash-dotted lines in (a) and (b) indicate the image planes of investigation for $x_2 = 0.95$, $x_1 = 0.35$, and $x_3 = 0.6$ m shown in Figures 7, 8, and 9, respectively. The dashed and dash-dotted lines in (c) indicate the horizontal and vertical sections intersecting objects A and F shown in Figures 10 and 11, respectively.

that are, respectively, 180° and approximately 90° out-of-phase with respect to the multicomponent results. Due to the different constants in the different imaging algorithms, the resultant amplitudes are expected to differ significantly. This is highlighted by the spatial resolution functions of Table 1, which show amplitudes proportional to $k/(2\pi)$, $C/(2k)$, and $-jC$ for the multicomponent, SAR, and Gazdag extrapolators, respectively. To aid the comparisons, the results of the different imaging algorithms are normalized with respect to the maximum absolute value provided by the multicomponent algorithm. The maximum absolute values for the multicomponent, SAR, and Gazdag imaging results were 149, 4.9×10^5, and 4.4×10^6, respectively. These values were obtained for the image of steel pipe B. For the comparisons, the images are viewed on different vertical and horizontal slices.

In Figure 7, the real, imaginary, and absolute values of the image contrasts are plotted for $x_2 = 0.95$ and $0.5 < x_1 < 3$, the vertical plane that intersects pipe A (see Figure 6a). The three imaging algorithms produce different contrasts. At a depth $x_3 = 0.55$ m (indicated by a black arrow), the multicomponent, SAR, and Gazdag images have mainly negative real-valued, positive real-valued and negative imaginary-valued contrasts, respectively. Artefacts on either side of the steel pipe are present on the SAR image (indicated by white arrows). These are probably a result of the fact that amplitudes for large horizontal wavenumbers are relatively large for the SAR algorithm [see equation (18)]. Gunawardena and Longstaff (1998) also show that conventional SAR algorithms are limited in widebeam applications, because they are not wave-equation based.

In Figure 8, the real, imaginary, and absolute values of the images are plotted for $x_1 = 0.35$ and $0 < x_2 < 3.5$ (see Figure 6a). This vertical plane intersects objects C, D, and E. Again the images are different (e.g., the amplitudes and phases for the targets differ for the different imaging algorithms). On the right side of Figure 8, the absolute values of images obtained with the multicomponent imaging algorithm are noticeably larger than those produced by the scalar imaging algorithms.

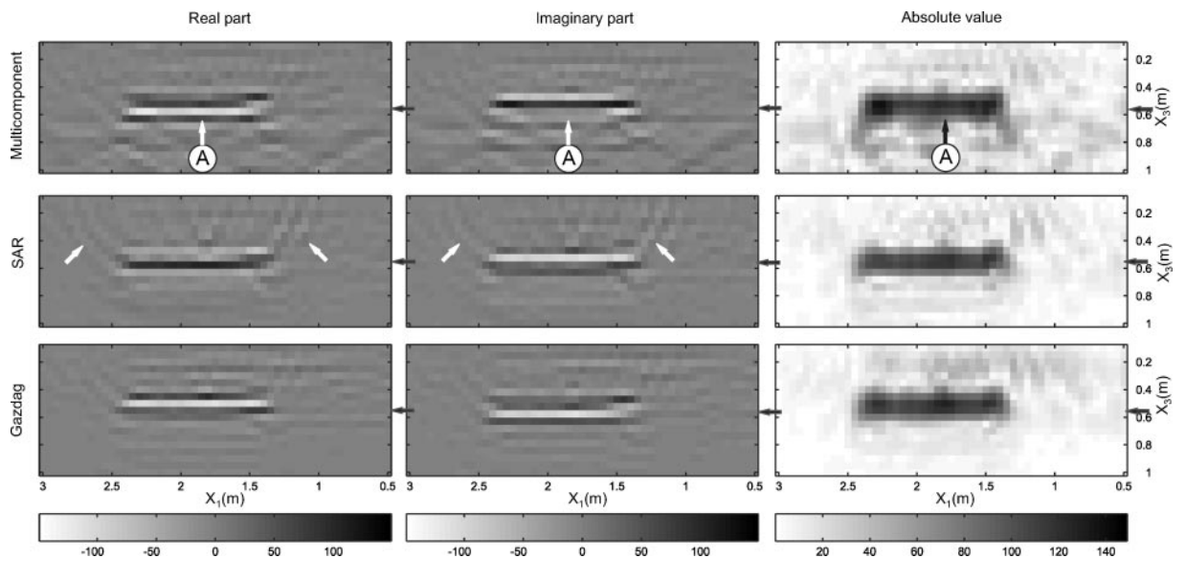

FIG. 7. Comparison of the real part (left), imaginary part (middle), and absolute values (right) of the images in Figure 6 for $x_2 = 0.95$ m. See text for explanation of arrows.

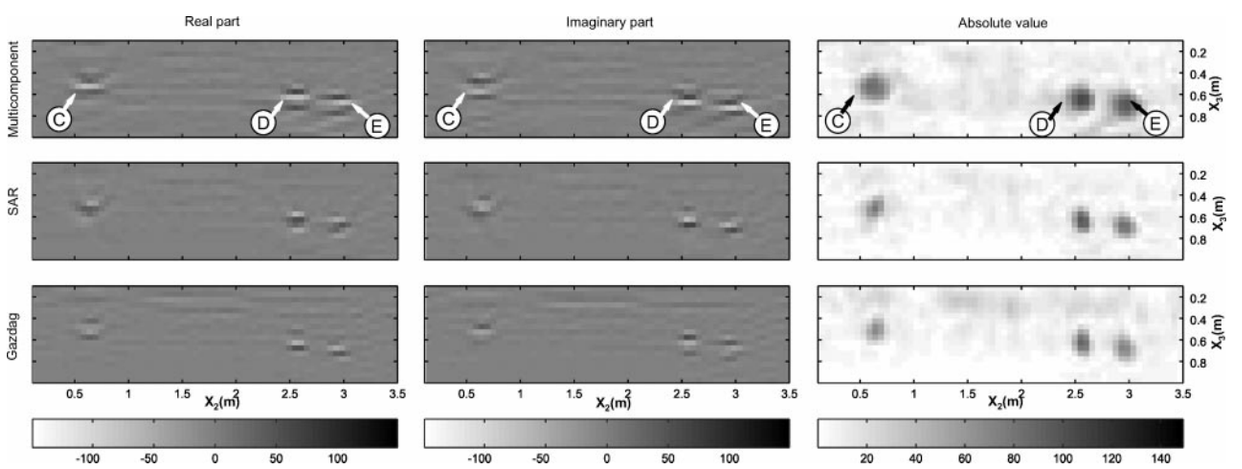

FIG. 8. Comparison of the real part (left), imaginary part (middle), and absolute values (right) of the images in Figure 6 for $x_1 = 0.35$ m.

In Figure 9, the real, imaginary, and absolute values of the images are plotted for $x_3 = 0.6$ m for the region bounded by $2.3 < x_2 < 3.8$ and $0 < x_1 < 3.2$ (see Figure 6b). This horizontal plane intersects objects D, E, and G. The amplitude of the image computed for the pipe G using the multicomponent imaging algorithm is larger than that obtained with the scalar imaging algorithms. This is probably due to the fact that the $\hat{E}_{21}$-component has its maximum response when both antennas are oriented 45° to the pipe (Daniels et al., 1988). Since we did not make measurements at $x_2 > 3.8$ m, the amplitudes of the image weaken on approaching the boundary of the sandbox. The multicomponent and SAR images for spheres D and E have the largest amplitude in the imaginary part of the images; sphere D and E have negative and positive imaginary-valued contrasts using the multicomponent algorithm, whereas they have a positive and negative imaginary-valued contrast using the SAR algorithm. By comparison, the Gazdag image has the largest amplitude in the real parts of the images for sphere D and E.

Comparison between the imaging algorithms along sections

Vertical and horizontal slices enable global comparisons between results produced by the different imaging algorithms to be made. An alternative insightful way to compare the different results is to plot the processed signals along vertical and horizontal sections that intersect the objects. Such an analysis is carried out here for the metal pipe A and the plastic sphere F. In Figure 10, the real, imaginary, and absolute values of images computed using the three imaging procedures are plotted. The three displayed sections intersect at object A [$\mathbf{x} = (1.95, 0.95, 0.55)$] and are parallel to the x_1, x_2, and x_3-axes, respectively (see dashed lines in Figure 6c). The intersection point is indicated by an arrow in each figure. These results highlight key information difficult to discern in Figure 7 for $x_3 = 0.55$, from which we have already observed that the SAR, Gazdag, and multicomponent images have mainly positive real-valued, negative imaginary-valued, and negative real-valued contrasts, respectively. Figure 10 confirms these observations for the respective maximum values, such that the SAR image has an opposite sign relative to the multicomponent image, and the Gazdag image has a 90° phase shift. These results agree with those obtained for the homogeneous and half-space synthetic computations.

In the left diagrams of Figure 10, the horizontal resolution of the multicomponent image is better than that of the scalar images, whereas in the middle diagrams of Figure 10, the horizontal resolution of the multicomponent image is slightly inferior to the scalar images. These results are similar to those obtained from our analysis of the spatial resolution functions in a homogeneous medium (Table 1).

In Figure 11, the real, imaginary, and absolute values of the derived images are plotted for three sections that intersect object F at position $\mathbf{x} = (1.45, 2.7, 0.55)$ (for locations see the dash-dotted lines in Figure 6c). Again, the intersection point is indicated by an arrow. For the multicomponent image, the amplitude of the peak in the imaginary part is markedly higher than that in the real part. The maximum values for the SAR and Gazdag images have a negative imaginary and a negative real-valued peak, respectively.

Due to the fact that the wavelet is not known in our study, it is not possible to obtain the physical properties of the object.

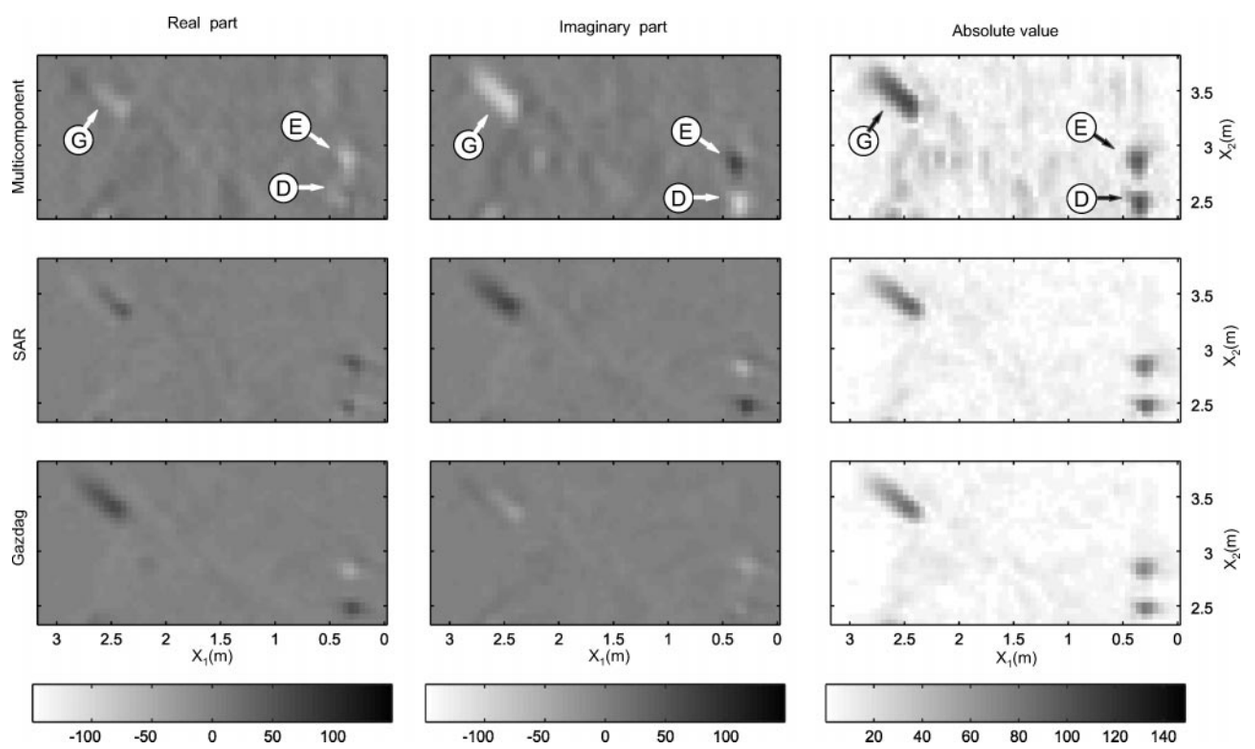

FIG. 9. Comparison of the real part (left), imaginary part (middle), and absolute values (right) of the images in Figure 6 for $x_3 = 0.6$ m.

However, the phase differences that occur in the experimental data are similar to those obtained in the synthetic analyses. We anticipate that when the source wavelet is known, an analysis that provides the medium properties can be carried out.

CONCLUSIONS

A multicomponent image reconstruction technique based on the electromagnetic vectorial wave equation has been derived. It accounts for all propagation effects, including the vectorial radiation characteristics of the source and receiver antennas and the polarization of the electromagnetic wave. The result of multicomponent imaging a point scatterer located in a homogeneous medium using a single frequency component (defined here to be the spatial resolution function) is circularly symmetric. Comparison of this result with those produced by the scalar SAR and the Gazdag imaging algorithms demonstrates the inadequacies of these algorithms; the scalar inverse wavefield extrapolators do not produce the required circular spatial resolution functions, indicating that the radiation characteristics of the source and receiver antennas influence the resultant images. Moreover, for a point scatterer with a real-valued contrast, the multicomponent image produces a real-valued peak, whereas the SAR and Gazdag images return negative real-valued and positive imaginary-valued peaks, respectively.

For a homogeneous half-space, it is not feasible to determine analytic solutions for the spatial resolution function. Fortunately, appropriate solutions can be determined numerically. Furthermore, numerical methods allow offsets between the source and receiver antennas to be taken into account. The

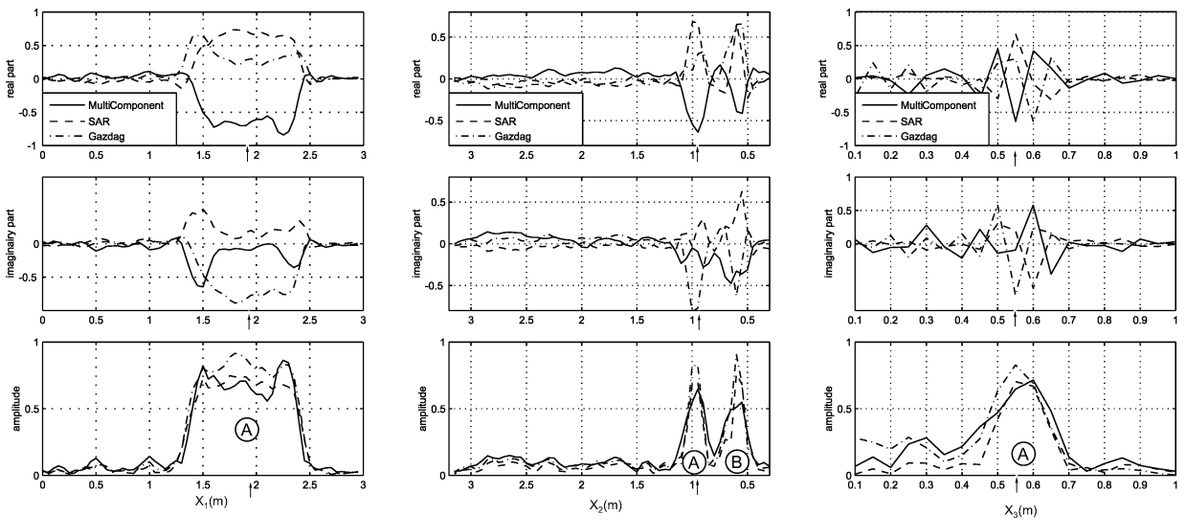

FIG. 10. Analysis of real and imaginary parts and absolute values of images for the metal pipe (A) along a line parallel to the x_1-axis (left), x_2-axis (middle), and x_3-axis (right). The arrows on the axes indicate the location of the point of intersection $\mathbf{x} = (1.95, 0.95, 0.55)$ m.

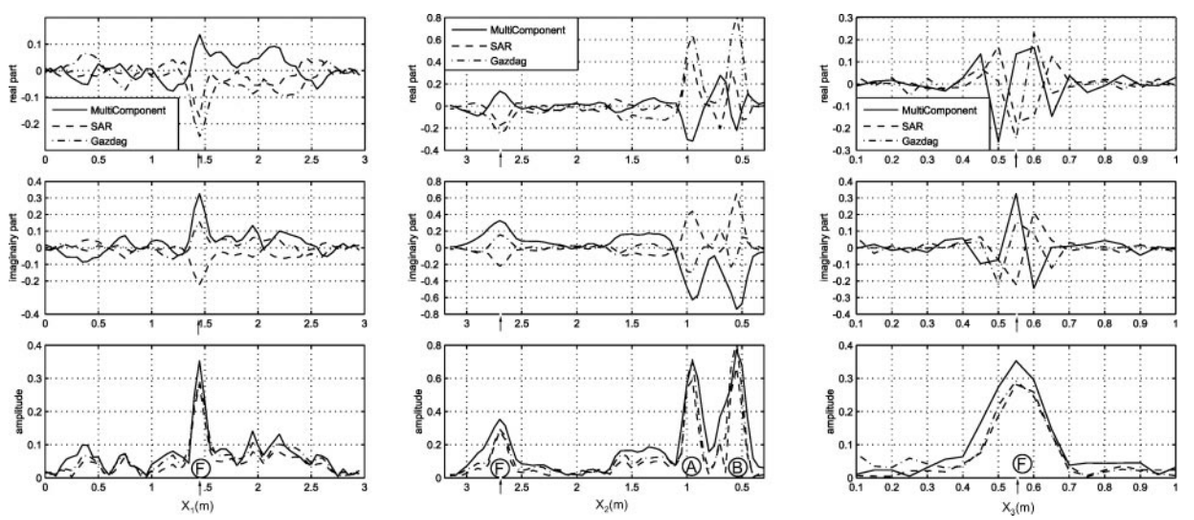

FIG. 11. Analysis of real and imaginary parts and absolute values of the images for the plastic sphere (F) along a line parallel to the x_1-axis (left), x_2-axis (middle), and x_3-axis (right). The arrows on the axes indicate the location of the point of intersection $\mathbf{x} = (1.45, 2.7, 0.55)$ m.

result of multicomponent imaging a point scatterer located in a homogeneous half-space is circularly symmetric and real-valued. Both scalar imaging algorithms produce noncircularly symmetric resolution functions for antennas overlying a half-space. Even though a positive real-valued contrast is used in the synthetic tests, the SAR extrapolator produces a negative real-valued peak and a significant nonzero imaginary-valued contrast, and the Gazdag extrapolator produces an imaginary-valued peak and a significant nonzero real-valued contrast. These results are similar to those obtained for a homogeneous medium.

Results of multicomponent and scalar imaging experimental data have been presented. For the multicomponent imaging, the radiation patterns of the source and receiver antennas overlying a homogeneous half-space and the offset between the antennas were taken into account. Several objects were correctly imaged. Again, the SAR images had an opposite sign compared with the multicomponent images, whereas the Gazdag images had a phase shift of 90° with respect to the multicomponent images. These results were analogous to those obtained for the point scatterer embedded within a homogeneous medium and a homogeneous half-space.

ACKNOWLEDGMENTS

This research has been supported by the Dutch Technology Foundation (STW), project nr. DMB 3649. The authors thank Alan Green for his constructive reviews of various versions of this manuscript and Peter Annan for inspiring discussions.

REFERENCES

Annan, A., Waller, W., Strangway, D., Rossiter, J., Redman, J., and Watts, R., 1975, The electromagnetic response of a low-loss two-layer, dielectric earth for horizontal electric dipole excitation: Geophysics, **40**, 285–298.
Binningsbø, J., Eide, E., and Hjelmstad, J., 2000, 3D Migration of GPR array-antenna data: 8th Internat. Conf. on Ground-Penetrating Radar (GPR), Expanded Abstracts, 459–463.
Bleistein, N., 1984, Mathematical methods for wave phenomena: Academic Press, Inc.
Claerbout, J., 1971, Toward a unified theory of reflector mapping: Geophysics, **36**, 467–481.
Curlander, J., and McDonough, R., 1991, Synthetic aperture radar, systems and signal processing: Wiley.
Daniels, D., Gunton, D., and Scott, H., 1988, Introduction to subsurface radar: IEE-Proc. Part F, **135**, 278–321.
Davis, J., and Annan, A., 1989, Ground-penetrating radar for high resolution mapping of soil and rock stratigraphy: Geophys. Prosp., **37**, 531–551.
Engheta, N., Papas, C., and Elachi, C., 1982, Radiation patterns of interfacial dipole antennas: Radio Sci., **17**, 1557–1566.
Gazdag, J., 1978, Wave equation migration with the phase-shift method: Geophysics, **43**, 1342–1351.
Grasmueck, M., 1996, 3-D ground-penetrating radar applied to fracture imaging in gneiss: Geophysics, **61**, 1050–1064.
Gunawardena, A., and Longstaff, D., 1998, Wave equation formulations of synthetic aperture radar (SAR) algorithms in the time-space domain: IEEE Trans. Geosci. Remote Sensing, **36**, 1995–1999.
Hansen, T., and Johansen, P., 2000, Inversion scheme for ground penetrating radar that takes into account the planar air-soil interface: IEEE Trans. Geosci. Remote Sensing, **38**, 496–506.
Johansson, E., and Mast, J., 1994, Three-dimensional ground penetrating radar imaging using synthetic aperture time-domain focusing: Proc. SPIE, **2275**, 205–214.
Lehmann, F., and Green, A., 1999, Semi-automated georadar data acquisition in three dimensions: Geophysics, **64**, 836–848.
Lehmann, F., Boerner, D., Holliger, K., and Green, A., 2000, Multicomponent georadar data: Some implications for data acquisition and processing: Geophysics, **65**, 1542–1552.
Lopez-Sanchez, J., and Fortuny-Guasch, J., 2000, 3-D Radar imaging using range migration techniques: IEEE Trans. Ant. Propagat, **48**, no. 5, 728–737.
Mast, J., and Johansson, E., 1994, Three-dimensional ground penetrating radar imaging using multi-frequency diffraction tomography: Proc. SPIE, **2275**, 196–203.
Moran, M., Greenfield, R., Arcone, S., and Delaney, A., 2000, Multidimensional GPR array processing using Kirchhoff migration: J. Appl. Geophys., **43**, 281–295.
van der Kruk, J., 2001, Three-dimensional imaging of multi-component ground penetrating radar data: Ph.D. thesis, Delft University of Technology (wwwtg.mp.tudelft.nl/~jvdkruk).
van Gestel, J., and Stoffa, P., 2000, Migration using multi-configuration GPR data: 8th Internat. Conf. on Ground-Penetrating Radar (GPR), Expanded Abstracts, 448–452.
Wang, T., and Oristaglio, M., 2000, GPR Imaging using the generalised Radon transform: Geophysics, **65**, 1553–1559.

APPENDIX A

FORWARD WAVEFIELD EXTRAPOLATOR IN A HOMOGENEOUS MEDIUM AND HOMOGENEOUS HALF-SPACE

In this appendix, the four different components of the forward wavefield extrapolator in a homogeneous medium and homogeneous half-space are derived in the space-frequency and wavenumber-frequency domains. In the main text, these four different components are combined in a matrix that forms the multicomponent forward wavefield extrapolator.

Space-frequency (x-ω) representation

For a homogeneous medium in which horizontal source and receiver antennas are present on the same horizontal plane, the Green's function $\hat{G}_{\alpha\ell}(\mathbf{x}^M|\mathbf{x}^c,\omega)$ can be written as $\hat{G}_{\alpha\ell}(\mathbf{x}^M-\mathbf{x}^c,\omega)$ and is given by

$$\hat{G}_{\alpha\ell}(\mathbf{x},\omega)=\hat{\eta}^{-1}\left[\partial_\alpha\partial_\ell+k^2\delta_{\alpha\ell}\right]\frac{\exp(-jkR)}{4\pi R}, \quad \text{(A-1a)}$$

$$R=|\mathbf{x}|, \quad \text{(A-1b)}$$

$$k=\frac{\omega}{c}, \quad \text{(A-1c)}$$

where c is the propagation velocity. The forward wavefield extrapolator for coincident source and receiver antennas can be rewritten by separating the amplitude and phase delay factors as

$$\begin{aligned}\hat{D}_{\alpha\beta}(\mathbf{x},\omega)&=\hat{G}_{\alpha\ell}(\mathbf{x},\omega)\hat{G}_{\beta\ell}(\mathbf{x},\omega),\\&=\hat{A}_{\alpha\beta}(\mathbf{x},\omega)\exp(-2jkR).\end{aligned} \quad \text{(A-2)}$$

Because the wavefield extrapolator in equation (A-2) is derived for zero-offset measurements, a factor of 2 occurs in the phase delay $\exp(-2jkR)$ to account for the two-way nature of the wavefield's travelpath. The separate elements of $\hat{A}_{\alpha\beta}$ in equation (A-2) can be evaluated for the far-field contributions using equations (A-1a)–(A-1c) as

$$\hat{A}_{11}(\mathbf{x},\omega)=\frac{R^2-x_1^2}{R^4}C(\omega), \quad \text{(A-3a)}$$

$$\hat{A}_{12}(\mathbf{x},\omega)=-\frac{x_1x_2}{R^4}C(\omega), \quad \text{(A-3b)}$$

$$\hat{A}_{21}(\mathbf{x},\omega)=-\frac{x_1x_2}{R^4}C(\omega), \quad \text{(A-3c)}$$

$$\hat{A}_{22}(\mathbf{x}, \omega) = \frac{R^2 - x_2^2}{R^4} C(\omega), \tag{A-3d}$$

where

$$C(\omega) = \frac{k^4}{\hat{\eta}^2 (4\pi)^2}. \tag{A-4}$$

For a homogeneous half-space, where the horizontal source and receiver antennas are present on the interface, the expression for the Green's function is much more complicated than for a homogeneous medium (Engheta et al., 1982). Nevertheless, the forward wavefield extrapolator in a homogeneous half-space for a zero-offset source-receiver pair located on the surface of the half-space can still be written as equation (A-2), but the amplitudes of $\hat{A}_{\alpha\beta}$ are much more complex than for a homogeneous medium.

Wavenumber-frequency (k-ω) representation

To determine the forward wavefield extrapolator in the wavenumber-frequency domain, a horizontal spatial Fourier transformation of $\hat{D}_{\alpha\beta}$ must be carried out. Using equation (A-2), we obtain

$$\begin{aligned}\tilde{D}_{\alpha\beta}(k_1, k_2, x_3, \omega) &= \int_{A(x_1,x_2)} \hat{D}_{\alpha\beta}(\mathbf{x}, \omega) \exp[j(k_1 x_1 + k_2 x_2)]\, \mathrm{d}A, \\ &= \int_{A(x_1,x_2)} \hat{A}_{\alpha\beta}(\mathbf{x}, \omega) \exp\left[\frac{j\omega\phi(\mathbf{x})}{c}\right] \mathrm{d}A,\end{aligned} \tag{A-5}$$

where

$$\phi(\mathbf{x}) = -2R(\mathbf{x}) + \frac{k_1}{k} x_1 + \frac{k_2}{k} x_2. \tag{A-6}$$

Using the method of stationary phase (Bleistein, 1984), equation (A-5) can be approximated for large ω as follows:

$$\tilde{D}_{\alpha\beta}(k_1, k_2, x_3, \omega) = \tilde{d}_{\alpha\beta}(k_1, k_2, x_3, \omega) \exp(-jk_3|x_3|), \tag{A-7}$$

where k_3 is given by

$$k_3 = \begin{cases} \sqrt{4k^2 - k_1^2 - k_2^2}, & \text{for} \quad k_1^2 + k_2^2 \le 4k^2, \\ -j\sqrt{k_1^2 + k_2^2 - 4k^2}, & \text{for} \quad k_1^2 + k_2^2 > 4k^2, \end{cases} \tag{A-8}$$

and

$$\tilde{d}_{11}(k_1, k_2, x_3, \omega) = -\frac{2\pi j C(\omega)}{(2k)^3 |x_3|}\left[(2k)^2 - k_1^2\right], \tag{A-9a}$$

$$\tilde{d}_{12}(k_1, k_2, x_3, \omega) = \frac{2\pi j C(\omega)}{(2k)^3 |x_3|} k_1 k_2, \tag{A-9b}$$

$$\tilde{d}_{21}(k_1, k_2, x_3, \omega) = \frac{2\pi j C(\omega)}{(2k)^3 |x_3|} k_1 k_2, \tag{A-9c}$$

$$\tilde{d}_{22}(k_1, k_2, x_3, \omega) = -\frac{2\pi j C(\omega)}{(2k)^3 |x_3|}\left[(2k)^2 - k_2^2\right]. \tag{A-9d}$$

For a homogeneous half-space, the horizontal wavefield extrapolator can still be written as equation (A-7), but as for the amplitudes $\hat{A}_{\alpha\beta}$, the amplitudes of $\tilde{d}_{\alpha\beta}$ are much more complex than for a homogeneous medium.

APPENDIX B

INDIVIDUAL (SCALAR) INVERSE WAVEFIELD EXTRAPOLATORS THAT INCORPORATE VECTORIAL RADIATION CHARACTERISTICS: SITUATION FOR A HOMOGENEOUS MEDIUM

Here, an attempt is made to derive inverse wavefield extrapolators for individual elements of the forward wavefield extrapolator that include the vectorial radiation characteristics. For simplicity, we treat the case of zero-offset source-receiver antennas in a homogeneous medium. Clearly, for correct formulation, the amplitudes must be bounded.

Although, exact solutions do not exist [inversions cannot be applied to the evanescent regions of the wavefield; see equation (A-8)], the individual-component wavefield extrapolators $\tilde{D}_{\alpha\beta}(k_1, k_2, x_3, \omega)$ in equations (A-7)–(A-9) are conveniently inverted in the $\mathbf{k}$-ω domain. On inverse Fourier transformation using the stationary-phase approximation, expressions for the individual inverse wavefield extrapolators $\hat{H}_{\alpha\beta}$ in the space domain are

$$\hat{H}_{11} = \frac{-R^2}{R^2 - x_1^2} \frac{\exp(2jkR)}{\pi^2 C(\omega)}, \tag{B-1a}$$

$$\hat{H}_{12} = \frac{-R^2}{x_1 x_2} \frac{\exp(2jkR)}{\pi^2 C(\omega)}, \tag{B-1b}$$

$$\hat{H}_{21} = \frac{-R^2}{x_1 x_2} \frac{\exp(2jkR)}{\pi^2 C(\omega)}, \tag{B-1c}$$

$$\hat{H}_{22} = \frac{-R^2}{R^2 - x_2^2} \frac{\exp(2jkR)}{\pi^2 C(\omega)}. \tag{B-1d}$$

Note, that the amplitude of $\hat{H}_{11}$ is not bounded when a scatterer is near the x_1-axis. In such a situation, noise will be amplified. This is caused by the fact that the radiation pattern of a horizontal dipole oriented in the x_1-direction has a zero along the x_1-axis [see equation (A-3a)]. Similarly, $\hat{H}_{12}$ and $\hat{H}_{21}$ are not bounded near $x_1 = 0$ or $x_2 = 0$, and $\hat{H}_{22}$ is not bounded near the x_2-axis [equations (B-1b)–(B-1d)]. In conclusion, individual-component inverse wavefield extrapolation based on the forward wavefield extrapolator $\hat{\mathbf{D}}_{\alpha\beta}$ for a homogeneous medium is generally not bounded.

Similar patterns occur for the homogeneous half-space and likely occur for an arbitrary heterogeneous medium. In a homogeneous half-space, zeros in the radiation characteristics occur at the interface in both the E-plane (plane parallel to the orientation of the dipole source) and H-plane (plane perpendicular to the orientation of the dipole source), and at the critical angle in the E-plane. These zeros will result in unbounded amplitudes for the scalar inverse wavefield extrapolator.

APPENDIX C

SPATIAL RESOLUTION FUNCTIONS IN A HOMOGENEOUS MEDIUM

In the following, we assume that zero-offset source-receiver antennas measure on a plane within a homogeneous medium. For the special situation of a single diffractor at position $\mathbf{x}^d$ having a real-valued (conductivity) contrast with unit amplitude

$$\chi(\mathbf{x}^c) = \delta(\mathbf{x}^c - \mathbf{x}^d), \tag{C-1}$$

where $\delta(x)$ is the spatial delta function, the measured electric field may be expressed in terms of the source function $\hat{S}(\omega)$ [see equation (6)] as

$$\hat{\mathbf{E}}(\mathbf{x}^M, \omega) = \hat{S}(\omega)\hat{\mathbf{D}}(\mathbf{x}^M - \mathbf{x}^d, \omega). \tag{C-2}$$

For convenience, we consider a source function that also has unit amplitude. The expression for the band-limited version of the contrast at depth x_3^d using the multicomponent inverse wavefield extrapolators is

$$\langle \hat{\chi}(\mathbf{x}, \omega)\mathbf{I}\rangle^{mc} = \int_{A\left(x_1^M, x_2^M\right)} \hat{\mathbf{H}}^{mc}(\mathbf{x} - \mathbf{x}^M, \omega) \times \hat{\mathbf{D}}(\mathbf{x}^M - \mathbf{x}^d, \omega)\,\mathrm{d}A, \quad \text{for} \quad x_3 = x_3^d, \tag{C-3}$$

where the inverse wavefield extrapolator $\hat{\mathbf{H}}^{mc}$ is given by equation (15). Using some basic results of Fourier theory, we may express equation (C-3) in terms of the Fourier transforms of $\hat{\mathbf{H}}^{mc}$ and $\hat{\mathbf{D}}$, such that

$$\langle \hat{\chi}(\mathbf{x}, \omega)\mathbf{I}\rangle^{mc} = \frac{1}{4\pi^2}\int_{(A(k_1,k_2)} \tilde{\mathbf{H}}^{mc}\left(k_1, k_2, x_3^d, \omega\right) \times \tilde{\mathbf{D}}\left(k_1, k_2, x_3^d, \omega\right) \times \exp\left[-j\left(k_1\left\{x_1 - x_1^d\right\} + k_2\left\{x_2 - x_2^d\right\}\right)\right]\mathrm{d}A, \quad \text{for} \quad x_3 = x_3^d, \tag{C-4}$$

where $\tilde{\mathbf{D}}$ is given by equation (11) and $\tilde{\mathbf{H}}^{mc}$ is given by equation (13). We can evaluate equation (C-4) by ignoring the contribution of the evanescent waves. This is achieved most conveniently by transforming the equations to polar coordinates r, ϕ, x_3 in the $\mathbf{x}$-ω domain. The corresponding transformed coordinates in the $\mathbf{k}$-ω domain are given by κ, θ, x_3. By suppressing the effects of the evanescent waves, the maximum radial spatial frequency component is $2k$. From equation (C-4), we obtain

$$\left\langle \hat{\chi}\left(r, \phi, x_3^d, \omega\right)\mathbf{I}\right\rangle^{mc} = \frac{1}{4\pi^2}\int_{\kappa=0}^{2k}\left(\int_{\theta=0}^{2\pi} \tilde{\mathbf{h}}^{mc}\left(\kappa, \theta, x_3^d, \omega\right) \times \tilde{\mathbf{d}}\left(\kappa, \theta, x_3^d, \omega\right)\exp[-j\kappa r\cos(\theta)]\,\mathrm{d}\theta\right)\kappa\,\mathrm{d}\kappa, \tag{C-5}$$

where we use the fact that for propagating waves, the exponentials in $\tilde{\mathbf{H}}^{mc}$ and $\tilde{\mathbf{D}}$ cancel, so that $\tilde{\mathbf{H}}^{mc}\tilde{\mathbf{D}} = \tilde{\mathbf{h}}^{mc}\tilde{\mathbf{d}}$. Evaluating $\tilde{\mathbf{h}}^{mc}\tilde{\mathbf{d}}$, which are given by equations (12) and (14), yields the unity matrix $\mathbf{I}$, because $\tilde{\mathbf{H}}^{mc}$ is the inverse of $\tilde{\mathbf{D}}$ for propagating waves. Evaluation of the integrals in equation (C-5) yields

$$\left\langle \hat{\chi}\left(r, \phi, x_3^d\right)\mathbf{I}\right\rangle^{mc} = \frac{2k}{2\pi}\frac{J_1(2kr)}{r}\mathbf{I}. \tag{C-6}$$

The multicomponent operator returns a real-valued circularly symmetric resolution function with a positive peak, thus yielding a satisfactory image of the point scatterer. Because the radiation charateristics of the source and receiver antennas and the vectorial character of the electromagnetic waves are taken into account, we obtain a circularly symmetric image for the point scatterer.

Substitution of the SAR and Gazdag inverse wavefield extrapolators, equations (17) and (19), respectively, for the inverse wavefield extrapolator in equation (21) and carrying out a similar analysis as in equations (C-4) and (C-5) yields

$$\hat{\chi}_{\alpha\beta}^{\{sar,gd\}}\left(r, \phi, x_3^d, \omega\right) = \frac{1}{4\pi^2}\int_{\kappa=0}^{2k}\left(\int_{\theta=0}^{2\pi} \tilde{h}^{\{sar,gd\}}\left(\kappa, \theta, x_3^d, \omega\right) \times \tilde{d}_{\alpha\beta}\left(\kappa, \theta, x_3^d, \omega\right)\exp[-j\kappa r\cos(\theta)]\,\mathrm{d}\theta\right)\kappa\,\mathrm{d}\kappa. \tag{C-7}$$

For the SAR inverse extrapolator, $\tilde{h}^{sar} = 4\pi jk|x_3|/(k_3^*)^2$ [see equation (17)] and $\tilde{d}_{11}$ [equation (A-9a)] must be substituted in equation (C-7). It is not feasible to obtain a closed-form expression for the resolution function. However, an angle-dependent resolution function is obtained that is independent of the depth of the diffractor (van der Kruk, 2001).

For the Gazdag phase shift extrapolator, $\tilde{h}^{gd} = 1$ [see equation (19)] and $\tilde{d}_{11}$ [equation (A-9a)] must be substituted into equation (C-7), yielding

$$\hat{\chi}_{11}^{gd}\left(r, \phi, x_3^d, \omega\right) = \frac{-jC(\omega)}{\left|x_3^d\right|}\left(\sin^2(\phi)\frac{J_1(2kr)}{r} + \left[3\cos^2(\phi) - \sin^2(\phi)\right]\frac{J_2(2kr)}{2kr^2}\right). \tag{C-8}$$

Analyzing this result in detail, we observe that the spatial resolution function is not circularly symmetric. Although the Gazdag filter is a symmetric extrapolator, the scattered wavefield has nonsymmetric properties [see also equations (A-2)–(A-3)]. Another drawback of this result is that the amplitude of the spatial resolution function is inversely proportional to the depth of the diffractor, whereas one would expect it to be independent of depth.